In vitro reconstitution of kinetochore–microtubule interface reveals a fundamental error correction mechanism

Doodhi, Harinath; Kasciukovic, Taciana; Gierlinski, Marek; Li, Shuyu; Clayton, Lesley; Tanaka, Tomoyuki U.

Published in:
BioRxiv

DOI:
10.1101/455873

Publication date:
2018

Document Version
Early version, also known as pre-print

In vitro reconstitution of kinetochore–microtubule interface reveals a fundamental error correction mechanism

Harinath Doodhi[1], Taciana Kasciukovic[1], Marek Gierlinski[1,2], Shuyu Li[1], Lesley Clayton[1] and Tomoyuki U. Tanaka[1]

1. Centre for Gene Regulation and Expression, School of Life Sciences, University of Dundee, Dow street, Dundee DD1 5EH, UK
2. Data Analysis Group, School of Life Sciences, University of Dundee, Dow street, Dundee DD1 5EH, UK

Abstract

For proper chromosome segregation, sister kinetochores must interact with microtubules from opposite spindle poles; this is called bi-orientation. To establish bi-orientation prior to chromosome segregation, any aberrant kinetochore–microtubule interaction must be resolved (error correction) by Aurora B kinase that phosphorylates outer kinetochore components. Aurora B differentially regulates kinetochore attachment to the microtubule plus end and its lateral side (end-on and lateral attachment). However, it is still unknown how kinetochore–microtubule interaction is turned over during error correction. Here we reconstituted the kinetochore–microtubule interface *in vitro* by attaching Ndc80 protein complexes (Ndc80Cs) to a nanobead that mimics the inner kinetochore. The Ndc80C–nanobeads recapitulated *in vitro* the lateral and end-on attachments of authentic kinetochores on dynamic microtubules loaded with the Dam1 complex. Using this system, we provide evidence that error correction is driven by direct competition for a kinetochore between the end-on attachment to one microtubule and the lateral attachment to another. We validated this competition-based error correction, using mathematical modelling and live-cell imaging. Our study reveals a fundamental mechanism of error correction, which contributes to efficient establishment of bi-orientation.

Introduction

For proper chromosome segregation, the kinetochore must interact with spindle microtubules (MTs) faithfully [1]. The kinetochore initially interacts with the lateral side of a single MT (lateral attachment) and is then tethered at the MT plus end (end-on attachment) [2-4]. Subsequently sister kinetochores form end-on attachments to MTs extending from opposite spindle poles, establishing chromosome bi-orientation. If an aberrant kinetochore–MT attachment is formed (Figure 1A, step 1), it must be resolved (error correction) by Aurora B kinase (Ipl1 in budding yeast), which phosphorylates kinetochore components and disrupts the end-on attachment (step 2) [5-7]. In budding yeast, the Dam1 complex (Dam1C) is the most important Aurora B substrate for error correction [8, 9]. While the end-on attachment is disrupted by the action of Aurora B, the lateral attachment is impervious to Aurora B regulation and therefore can still be formed efficiently, allowing fresh kinetochore–MT attachment, during error correction (step 3, 4) [9]. Lateral attachment is then converted to end-on attachment; if this forms aberrantly it must be resolved again by Aurora B (step 1), but if bi-orientation is formed, tension across sister kinetochores stabilizes end-on attachment (step 5).

However, we are still far from understanding how the actual turnover of kinetochore–MT interactions takes place during error correction. It is generally thought that the kinetochore transiently becomes unattached to any MTs by the action of Aurora B during error correction (Figure 1A, step 2, sister kinetochore on right). Indeed, Dam1 phospho-mimetic mutants at Aurora B phosphorylation sites generate unattached kinetochores, which provides the evidence that end-on attachment is weakened [9, 10]. However, the generation of unattached kinetochores was rather a slow process [9] and its kinetics may not be physiologically relevant. If unattached kinetochores were indeed generated and this happens simultaneously to both sister kinetochores (step 6), then a sister chromatid pair would move away from the spindle and have to be re-caught on spindle MTs (step 7). This might delay the establishment of bi-orientation. There may be a way to allow error correction without generating unattached kinetochores. However, it is unknown how this can be achieved.

It has been difficult to study error correction process further *in vivo*, since MT density is extremely high between two spindle poles, making it improbable to directly visualize turnover of kinetochore–MT interaction during error correction in live cells. Here, to obtain more insight into the error correction process, we reconstituted the interface of kinetochore–MT interaction *in vitro* (i.e. in cell-free system) using defined recombinant kinetochore components.

Results

Reconstitution of kinetochore–MT interface *in vitro* using defined outer kinetochore components

The inner kinetochore supports assembly of Ndc80 complexes (Ndc80Cs) that extend outwards and directly bind MTs [11-13]. In budding yeast, the size of the inner kinetochore is estimated to be 50–70 nm [14]. To reconstitute the kinetochore–MT interface *in vitro*, we replaced the inner kinetochore with a nanobead of similar size (100 nm), and used purified outer kinetochore components Dam1C and Ndc80C. The Ndc80C containing the Spc24 component fused with GFP (Ndc80C-GFP) was expressed in, and purified from, insect cells (Figure 1B). In addition, Dam1C and Dam1C-GFP (in which the Dad1 component was fused with GFP) were expressed in, and purified from, bacterial cells (Figure 1B). Ndc80C-GFP was then attached to a streptavidin-coated nanobead through the biotinylated anti-GFP nanobody (Ndc80C–nanobead; Figure 1C, top), with the Ndc80C MT-binding domains oriented outward from the bead surface. Based on GFP intensity, we estimated that four Ndc80C-GFP molecules, on average, were attached to a single nanobead (Figure S1A). This was similar to a single purified kinetochore that had five presumable Ndc80Cs on it [14]. Dynamic MTs were generated *in vitro* from GMPCPP-stabilized MT seeds immobilized on coverslips, and observed by TIRF microscopy (Figure 1C, bottom). The Dam1C-GFP was able to track the end of depolymerizing MTs and accumulate there (up to 10-30 fold) (Figure S1B), as reported previously [4, 15].

Next, we investigated how Ndc80C (with GFP) nanobeads behave with dynamic MTs and Dam1C (without GFP) *in vitro*. An Ndc80C–nanobead first attached to the lateral side of a MT (lateral attachment) (Figure 1D). When the laterally-attached MT depolymerized and its plus end caught up with the Ndc80C–nanobead, the nanobead became tethered at the plus end of the MT and subsequently tracked this MT end as it continued to depolymerize (end-on attachment) (Figure 1D). Thus, the Ndc80C–nanobead recapitulated *in vitro* the behaviour of an authentic kinetochore in conversion from the lateral to end-on attachment on a single MT *in vivo* (i.e. within cells) [3, 4]. In the presence of Dam1C, the end-on attachment continued in 96% cases (Figure 1D, F). In the absence of Dam1C, the end-on attachment could still be formed, but the Ndc80C–nanobead often (30% cases) detached from the MT plus end following transient end-on interaction (Figure 1E, F), suggesting that Dam1C stabilizes end-on attachment. This is consistent with the important roles of Dam1C in formation of end-on attachment of an authentic kinetochore to a MT *in vivo* [4, 9].

Transfer of an Ndc80C–nanobead from one MT to another gives insight into the kinetochore–MT error correction process

During the kinetochore–MT error correction, kinetochores change their associated MTs (Figure 1A). This is a crucial process in error correction but it has been very difficult to visualize and analyze this exchange *in vivo* because of the high MT density on the mitotic spindle. This prompted us to investigate how Ndc80C–nanobeads change their associated MTs *in vitro*. For this, we observed situations where two MTs cross each other, one of which has an end-on attachment to an Ndc80C–nanobead during depolymerization (MT crossing assay; Figure 2A). This assay has two possible outcomes: the end-on attachment may continue and the Ndc80C–nanobead passes across the other MT (Figure 2A, blue rectangle). Alternatively, the Ndc80–nanobead may be transferred from the end of the original MT to the lateral side of the other MT as the depolymerizing MT crosses it (Figure 2A, orange rectangle).

We conducted the MT crossing assay in the presence and absence of Dam1C (Figure 2B, C). In the presence of Dam1C, the end-on attachment continued in most cases (97%) while the Ndc80C–nanobead passed the other MT (Figure 2B, D). By contrast, in the absence of Dam1C, in most cases (83%) the Ndc80 nanobead was transferred to the side of the other MT (Figure 2C, D). Given that Dam1C accumulates at the end of depolymerizing MTs, this difference can be explained by a weakened end-on attachment in the absence of Dam1C (Figure 1E). As a result, the affinity to the lateral attachment may surpass that to the end-on attachment, causing transfer of the Ndc80C–nanobead to the lateral side of another MT.

The Dam1C is the most important Aurora B substrate for error correction [8, 9] and its phosphorylation sites are clustered at the C-terminus of Dam1. It is thought that error correction continues while Dam1C is phosphorylated, and stops when bi-orientation is established and Dam1C is dephosphorylated [16]. To investigate how Dam1C phosphorylation by Aurora B affects kinetochore–MT interaction *in vitro*, we expressed Dam1C carrying phospho-mimetic mutations at the C-terminus of Dam1 in bacteria. The purified mutant Dam1Cs were called Dam1C-4D-GFP and Dam1C-4D, with and without GFP fusion to Dad1, respectively (Figure 2E). Dam1C-4D-GFP tracked the plus end of a depolymerizing MT and accumulated there (Figure S2A), as did Dam1C (wild-type)-GFP (Figure S2B). Crucially, Dam1C-4D was able to support continuous end-on attachment of Ndc80C–nanobeads in most cases without causing their detachment from the MT ends, as was Dam1C wild-type (Figure S2C). This result raises the possibility that Dam1C phosphorylation by Aurora B does not generate kinetochores lacking MT attachment

(unattached kinetochores). Then, how does Aurora B promote turnover of kinetochore-associated MTs during error correction?

To address this question, we used Dam1C-4D in the MT crossing assay (Figure 2A). In the presence of Dam1C-4D, the Ndc80C–nanobead was transferred from the plus end of one MT to the lateral side of another MT, in 41% cases (Figure 2F, G). When such transfer happened, the Ndc80C–nanobead was directly transferred from one MT to another, i.e. at least one MT was always attached to the nanobead, either end-on or laterally. It appears that, when an end-on attachment to one MT comes into direct competition with a lateral attachment to another MT, the Dam1C phosphorylation plays a key role in determining which attachment subsequently prevails. If the transfer of an Ndc80C–nanobead mirrors turnover of kinetochore-associated MTs *in vivo* during error correction, such turnover may proceed without generating unattached kinetochores.

Next, we measured the angle between the two MTs, when an Ndc80C–nanobead was transferred from the end of one MT to the lateral side of another in the presence of Dam1C-4D. The two MTs crossed with a wide variety of angles ranging from 27° to 152° (Figure S2D). However, when this angle was zero, i.e. when two MTs overlapped with the same orientation, an Ndc80C–nanobead was not transferred from the end of one MT to the lateral side of another (Figure S2E). We reason that, when two MTs overlap and a nanobead maintains the original end-on attachment, the nanobead may simultaneously form a lateral attachment to the other MT and can move along it with a low frictional drag (Figure S2F, top). In such circumstance, a sufficient force would not be generated to disrupt the original end-on attachment. This explains why Ndc80C–nanobeads were not transferred between overlapping MTs. By contrast, when MTs do not overlap (and their angle is not close to zero), the drag is greater due to MT rigidity, leading to disruption of the original end-on attachment (Figure S2F, bottom). An implication for error correction *in vivo* is that a kinetochore can change its associated MTs if these MTs extend from the opposite spindle poles, but cannot if they are from the same spindle pole.

Evidence that phosphorylation of the Dam1 C-terminus by Aurora B kinase disrupts interaction between Dam1C and Ndc80C during error correction

How could the Dam1 C-terminus phospho-mimetic mutants promote transfer of an Ndc80C–nanobead from the end of one MT to the lateral side of another in the MT crossing assay (Figure 2F, G)? The Dam1 C-terminus physically interacts with Ndc80C and its phosphorylation (or phospho-mimetic mutants) weakens this interaction [9, 17-19]. However, it was reported that the Dam1 C-terminus also interacts with MTs and its phosphorylation (or

phospho-mimetic mutants) weakens this interaction too [20, 21]. Therefore, phospho-mimetic mutants at the Dam1 C-terminus could disrupt either Dam1C–Ndc80C interaction or Dam1C–MT interaction to promote the transfer of an Ndc80C–nanobead between MTs.

To identify the point of disruption, we attached His-tagged Ndc80Cs (no GFP; Figure 3A) to nanobeads (which are visible with fluorescence) using a biotinylated anti-His antibody (Figures 1C). We then compared the behaviour of Dam1C-GFP and Dam1C-4D-GFP (Figures 1B, 2E) in the MT crossing assay (Figure 3B). The end-on attachment continued in most cases with Dam1 (wild-type)-GFP (Figure 3B, C), as with Dam1C (wild-type, no GFP fusion) (Figure 2B, D). Moreover, Ndc80C nanobeads was often transferred to the lateral side of another MT with Dam1C-4D-GFP (Figure 3B, D), as with Dam1C-4D (no GFP fusion) (Figure 2F, G). Soon after this transfer, we investigated the location of Dam1C-4D-GFP (Figure 3B, E). If the Dam1C–Ndc80C interaction were disrupted by Dam1 phospho-mimetic mutants, Dam1C-4D-GFP signals would continue tracking the end of a depolymerizing MT, moving away from the Ndc80C–nanobead that has been transferred to the side of another MT (Figure 3E, left). Alternatively, if the Dam1–MT interaction were disrupted by Dam1 phospho-mimetic mutants, the Dam1C-4D-GFP would remain on the Ndc80C–nanobead after it is transferred to the lateral side of another MT (Figure 3E, right).

In all the cases where Ndc80C–nanobeads were transferred to the side of another MT, Dam1C-4D-GFP signals continued tracking the end of a depolymerizing MT, moving away from the Ndc80C–nanobead (Figure 3D, E). For comparison, we looked at the location of Ndc80C-GFP signals soon after transfer of a nanobead to the side of another MT in the presence of Dam1C-4D (without GFP fusion) (Figure 2F); in all these cases, Ndc80C-GFP signals remained on nanobeads after this transfer (Figure 3E). Thus, we conclude that phospho-mimetic mutants at the Dam1 C-terminus disrupt the Dam1C–Ndc80C interaction, rather than the Dam1C–MT interaction, to promote transfer of an Ndc80C–nanobead from the end of one MT to the lateral side of another. This implicates that phosphorylation of Dam1 C-terminus by Aurora B kinase disrupts the end-on attachment specifically by weakening interaction between Dam1C and Ndc80C during kinetochore–MT error correction.

Testing two possible models for error correction using mathematical simulation and live-cell imaging

We have two possible models for error correction (Figure 4A): In the first model, the error correction proceeds through generation of unattached kinetochores (Model 1), as conventionally thought (Figure 1A). In the second model, the error correction proceeds through direct competition between end-on and lateral attachment (Model 2), as suggested

by the MT crossing assay *in vitro* (Figure 2). Based on each model, we developed a mathematical simulation, which consists of the sequence of states (Figure 4A, S3A). In Model 1, the end-on attachment is disrupted by the action of Aurora B kinase during syntelic attachment (both sister kinetochores interacting with MTs from the same pole) leading to generation of an unattached kinetochore (Figure 1A). An unattached kinetochore subsequently forms a lateral attachment, which is then converted to an end-on attachment. If the end-on attachment generates syntelic attachment again, the error correction continues. However, if it establishes bi-orientation, it is stabilized and the error correction stops. In Model 2, during syntelic attachment one kinetochore temporarily forms both the end-on and lateral attachments (Figure 1A). If these two attachments are to MTs from the same pole, the original end-on attachment remains. However, if they are to MTs from opposite poles, the original end-on attachment is disrupted and taken over by a new lateral attachment, i.e. direct competition occurs. When this lateral attachment is converted to an end-on attachment, bi-orientation is formed and error correction stops.

In the simulation, each transition between states occurred stochastically, and the time required for this transition was defined by a transition rate R (Figure 4A, S3A). We estimated a value of each R as follows: The rate of forming the lateral attachment (R_{form} and R_{rep} in Model 1 and 2, respectively) was estimated as 2 per min, based on live-cell imaging data of kinetochore capture by MTs [22]. The rate defining the duration of MT competition in Model 2 (R_{KO}) was estimated as 10 per min since an Ndc80C–nanobead maintained both end-on and lateral attachment for 4–8 seconds before end-on attachment is disrupted in the presence of Dam1C-4D (Figure 2F). The conversion rate from lateral to end-on attachment (R_{conv}) was estimated as 2 per min (Figure S3B), based on simulations used in our previous studies [22, 23]. The disruption rate of an end-on attachment (R_{det}), which generates an unattached kinetochore in Model 1, was difficult to estimate; so we optimized this value and found that R_{det}=1 per min achieves most efficient bi-orientation in the current simulation (Figure S3C). Based on these values, 10,000 simulations were run for each model; each simulation started with syntelic attachment, which is probably dominant when the bipolar spindle is initially formed ([5]; see below). The representative examples of the chain of states in simulations are shown in Figure S3D. The time required for establishing bi-orientation in simulations is shown for each model in Figure 4B; the median time was 3.0 and 1.8 min in Model 1 and 2, respectively.

To test the plausibility of each model, we next measured the time required for establishing bi-orientation *in vivo* by live-cell imaging (Figure 4C). We visualized spindle pole bodies (SPBs) and a chosen centromere (*CEN5*) in yeast cells, and observed their behaviour. In most cases, *CEN5* located in the vicinity of one SPB immediately after SPB separation (i.e.

establishment of a bipolar spindle). Typically, 1–3 min later, sister *CEN5* showed separation, or *CEN5* moved to the middle between two SPBs followed by sister *CEN5* separation; such an event was marked as establishment of bi-orientation, if sister *CEN5* separation continued thereafter (Figure S4A). Time required for bi-orientation after SPB separation is plotted in Figure 4D; the median time was 1.5 min. We compared this result with the simulation results of Model 1 and 2; the live-cell imaging result was consistent with Model 2, but not with Model 1 (Figure 4B, D). Therefore, we conclude that Model 2 is more plausible than Model 1, i.e. it is likely that error correction is driven by direct competition for a kinetochore between an end-on attachment to one MT and a lateral attachment to another (Figure 4E).

Discussion

In this study, we reconstituted the kinetochore–MT interface using recombinant Ndc80C and Dam1C. We replaced the inner kinetochore with a nanobead, onto which Ndc80C was attached with its MT-binding domain facing outward. The Ndc80C–nanobead interacted with the lateral side of a dynamic MT, subsequently attached to the MT end, and tracked it during MT depolymerization (Figure 1). Thus, the Ndc80C–nanobead showed conversion from lateral to end-on MT attachment on the same MT, as does the authentic kinetochore [4, 24]. The stability of the end-on attachment relied on Dam1C that also tracked the end of a depolymerizing MT. This system was then used to analyse the transfer of a kinetochore from a MT plus end to another MT, which is a key process during error correction but cannot be visualized *in vivo* because of the high density of MTs on the spindle. In the presence of Dam1C wild-type (non-phosphorylated *in vitro*), the Ndc80–nanobead was not transferred from the MT end to another MT. By contrast, with Dam1C phospho-mimetic mutants (at Aurora B sites), Ndc80C–nanobeads were often directly transferred from the MT plus end to the side of another MT that crossed the original MT (Figure 2). During this transfer process, at least one MT maintained attachment to the Ndc80C–nanobead; thus kinetochores that were unattached to any MTs were not generated.

How does the Dam1C phospho-mimetic mutants cause transfer of the Ndc80C–nanobead from the MT end to the lateral side of another MT? The interaction between Ndc80C and Dam1C configures the kinetochore–MT end-on attachment [4, 25]. With non-phosphorylated Dam1C (wild-type Dam1C *in vitro*), the end-on attachment is robust and prevails over the lateral attachment when they compete for an Ndc80C–nanobead (Figure 2). However, Dam1C phosphorylation (or phospho-mimetic mutants) weakens the Ndc80C–Dam1C interaction and therefore weakens the end-on attachment (Figure 3) [9, 17, 18]. On the other hand, Dam1C phosphorylation (or phospho-mimetic mutants) does not affect kinetochore attachment to the MT lateral side (lateral attachment) [9]. We therefore reason that the Dam1C phospho-mimetic mutants change the relative strength between lateral and end-on attachment such that lateral attachment prevails over end-on attachment (Figure 2). This allows transfer of the Ndc80C–nanobead from the MT end to the lateral side of another MT when the two MTs compete for the nanobead. Without competing lateral attachment, Ndc80C–nanobeads hardly detached from the ends of depolymerizing MTs in the presence of Dam1C phospho-mimetic mutants (Figure S2C). Thus, although the Dam1C phospho-mimetic mutant weakens the Ndc80C–Dam1C interaction, this is insufficient for disruption of end-on attachment, in the absence of competition with the lateral attachment to another MT.

In the absence of tension across sister kinetochores due to aberrant kinetochore–MT interactions, Dam1 stays phosphorylated by Aurora B *in vivo*, which is crucial for error correction [8, 16]. The behaviour of Ndc80C–nanobeads in MT crossing assay in the presence of phospho-mimetic Dam1C suggests that the error correction for authentic kinetochores could also proceed through direct competition between the end-on attachment to one MT and lateral attachment to another (Figure 4E). We developed mathematical models based on this direct competition (Figure 4A, Model 2), and also based on the conventional assumption that unattached kinetochores are generated during error correction (Figure 4A, Model 1). Using the two models, we derived the time required for bi-orientation. The model with direct competition, but not the model with generation of unattached kinetochores, was able to reproduce time required for bi-orientation in cells as observed by live-cell imaging (Figure 4D). Thus it is plausible that error correction proceeds through direct takeover of an end-on attachment by a lateral attachment (Figure 4E). This mechanism of direct competition contributes to more efficient establishment of bi-orientation, compared with the conventional model. Thus, our study reveals a novel kinetochore–MT error correction mechanism that ensures bi-orientation and proper chromosome segregation during mitosis.

Acknowledgements

We thank Tanaka lab members, E.R. Griffis, R. Cross, D. Peet, T. Surrey, G. Ball, E.A. Katrukha and M. Miller for discussion, S. Harrison, T. Davis, T. Richmond, K. Nakayama, L. Garcia and Addgene for reagents; E.R. Griffis, S. Swift, P. Appleton, D. Bajer and Dundee Imaging Facility for TIRF microscope setting and maintenance; N. Sheidaei for help in protein purification; and the OMERO team for technical help. This work was supported by the Wellcome Trust (096535, 097945) and Medical Research Council (K015869). T.U.T. is a Wellcome Trust Principal Research Fellow. The authors declare no competing financial interests.

Methods

Plasmid constructs

To express and purify *S. cerevisiae* Ndc80C-GFP, *NDC80, GST-NUF2, SPC24-GFP* and *SPC25* were cloned into Multibac vectors, pFL (*NDC80* and *GST-NUF2*) and pUCDM (*SPC24-GFP* and *SPC25*) [26]. A PreScission cleavage site was inserted between *GST* and *NUF2*. The two plasmids were then fused by Cre-lox recombination *in vitro*. After transfection of the plasmid containing all four components of Ndc80C into DH10MultiBac *E. coli* [26]. bacmid DNA was prepared using the alkaline lysis method. To express and purify Ndc80C (without GFP) with His tag (Ndc80C-His), *SPC24-His* was cloned instead of *SPC24-GFP*. The MultiBac system was a gift from Prof. Tim Richmond.

To express *S. cerevisiae* Dam1C and Dam1C-GFP components in *E. coli*, plasmid constructs were obtained from Prof. Stephen Harrison and Prof. Trisha Davis [27, 28], respectively. These constructs express Spc34 tagged with His at its C-terminus. To express Dam1C-4D and Dam1C-GFP-4D components, plasmid constructs were generated by DNA synthesis (DC Biosciences, Dundee) and cloning to replace four serine residues at C-terminus of Dam1 (serines at 257, 265, 292, 327 positions of Dam1) with aspartates [8, 9].

Protein purification

Bacmid DNA with Ndc80C components was transfected into Sf9 insect cells to produce baculovirus. For protein expression, Sf9 cells were grown for 60 to 72 hrs at 27 °C. The cells were then harvested and washed with PBS (8 mM NaHPO, 2mM KHPO, 2.7mM KCl, 137mM NaCl, pH7.4) and stored at -80 °C. For purification of Ndc80C proteins, the cells were resuspended in buffer containing 50 mM Hepes pH 7.4, 300 mM NaCl, 1 mM EDTA, 10% Glycerol, 1% Triton X-100, 1 mM DTT and protease inhibitor cocktail (Roche), and lysed with a Dounce homogenizer and sonication at 4 °C. The cell lysate was clarified by centrifugation at 25 000 x g for 45 to 60 min. The soluble fraction was bound to the GST Sepharose 4B (GE Healthcare) for 90 to 120 min at 4 °C. The unbound fractions were removed on a gravity flow column and washed with buffer containing 50 mM Hepes pH 7.4, 250 mM NaCl, 1 mM EDTA, 10% Glycerol and 1 mM DTT. The proteins were eluted in buffer containing 50 mM Hepes pH 7.4, 150 mM NaCl, 1 mM EDTA, 0.05% Triton X-100 and 1 mM DTT, by cleavage with PreScission protease (GE Healthcare) which cleaves between GST and Nuf2 in the GST-Nuf2 fusion protein. The eluted proteins were further purified by gel filtration using Superose 6 Increase 10/300 GL column (GE Healthcare) equilibrated with buffer containing 25 mM Tris-Cl pH 7.6, 250 mM NaCl, 1 mM EDTA, 3 mM $MgCl_2$, 5% Glycerol and 1mM DTT. The fractions containing Ndc80C were pooled, and the buffer was exchanged into the one containing 80 mM Pipes pH 6.8, 1 mM $MgCl_2$, 1 mM EGTA, 150 mM KCl, 5% sucrose and 0.2 mM DTT, using a PD-10 desalting column (GE Healthcare). Purified Ndc80C was stored at -80°C.

For purification of Dam1C proteins, Rosetta™ 2(DE3) cells (Novagen 71401) transformed with respective constructs were grown at 37 °C until OD_{600} reached 0.6–0.7. Then protein expression was induced by 0.1 mM IPTG for 22 hrs at 15-16 °C. The cells were harvested and stored at –80 °C. Dam1C proteins were purified in a three-step process, by affinity, ion-exchange and gel filtration chromatography as described [27]. The bacterial cells were resuspended in ice-cold buffer containing 50 mM sodium phosphate pH 7.5, 500 mM NaCl, 1 mM EDTA, 0.5% Trition X-100, 20 mM imidazole, 1 mM DTT and protease inhibitor cocktail (Roche). Cells were then lysed on ice and sonicated at 4°C, and the cell debris was separated by centrifugation at 25 000 x g for 45–60 min. The supernatant was incubated with Ni-NTA agarose (Qiagen) at 4 ºC for 90 min. Unbound fractions were separated using a gravity flow column. Protein-bound Ni-NTA agarose was washed with buffer containing 50 mM sodium phosphate pH 7.5, 500 mM NaCl, 1 mM EDTA, 0.5% Trition X-100, 50 mM imidazole and 1 mM DTT. Then proteins were eluted with the same buffer containing 250 mM imidazole without Triton X-100. The eluted proteins were exchanged into 50 mM sodium

phosphate pH7.5, 100 mM NaCl, 1 mM EDTA, 0.2 mM DTT by using PD-10 desalting columns (GE Healthcare), then 1 mM ATP and 250-fold molar excess of synthetic peptide NRLLTG was added and incubated for 1 h at 4 °C. Proteins were purified on a MonoQ 5/50 column (GE Healthcare) with a gradient of 100 to 1000 mM NaCl. The eluent was mixed again with 1 mM ATP and NRLLTG peptide (250-fold molar excess) and incubated for 1 h at 4 °C and purified on a Superose 6 Increase 10/300 GL column (GE Healthcare) equilibrated with 25 mM sodium phosphate pH7.4, 500 mM NaCl, 1 mM EDTA and 0.2 mM DTT. The fractions corresponding to Dam1C proteins were pooled and the buffer was exchanged into the one containing 80 mM PIPES pH 6.8, 1 mM $MgCl_2$, 1 mM EGTA, 150 mM KCl, 5% sucrose and 0.2 mM DTT. Purified Dam1C was stored at -80 °C.

Attaching Ndc80C to nanobeads

Fluorescent (excitation at 647 nm) streptavidin-coated magnetic nanobeads (100 nm diameter; will be referred as nanobeads hereafter) were obtained from Creative Diagnostics, USA (cat No.WHM-ME647). Ndc80C-GFP and Ndc80C-His were attached to nanobeads using biotinylated anti-GFP nanobody (see next paragraph) and biotinylated anti-His antibody (Quiagen cat No. 34440), respectively, as shown in Figure 1C (top). For this, the beads were incubated with biotinylated anti-GFP nanobody (or biotinylated anti-His antibody) for about 1 h along with 5 mg/mL BSA at 4 °C. The unbound fractions were removed after the nanobeads were bound to the magnet and washed three times in MRB80 buffer (80 mM Pipes pH 6.8, 1 mM $MgCl_2$, 1 mM EGTA) supplemented with 5 mg/ml BSA. The nanobeads were then incubated with Ndc80C in MRB80 buffer supplemented with 5 mg/ml BSA for 1 h at 4 °C, washed three times and finally resuspended in MRB80 buffer.

Biotinylated anti-GFP nanobody was produced as follows: AviTag DNA was cloned at the C-terminus of GST-anti-GFP-nanobody on the pGEX6P1-GFP-nanobody plasmid (Addgene, cat No. 61838; a gift from Prof Kazuhisa Nakayama) [29, 30]. GST-anti-GFP-nanobody-AviTag was expressed in BL21-gold (DE3) pLysS *E. coli* (Agilent Technologies 230134) and purified using glutathione-Separose beads (GE Healthcare). GST was removed from the protein while bound to glutathione beads using PreScission protease (GE Healthcare). Anti-GFP-nanobody-AviTag was biotinylated using recombinant Bir1 (Abcam, cat No. ab135015) in a reaction containing biotin and ATP, and biotinylation was confirmed in gel-shift analyses by SDS-PAGE, as described previously [29].

Generation of dynamic MTs on coverslips

Purified tubulin proteins were obtained from Cytoskeleton, Inc. For preparation of MT seeds, 20 µM of porcine tubulin mix containing 18% biotinylated tubulin, 12% rhodamine-labelled tubulin and 70% unlabelled tubulin was incubated with 1 mM guanylyl-(α,β)-methylenediphosphonate (GMPCPP) on ice and subsequently at 37 °C for 30 min. MTs were separated from free tubulin by centrifugation using an Airfuge (Beckman Coulter) for 5 min. The MTs were subjected to another round of depolymerization and polymerization with 1 mM GMPCPP, and the final MT seed samples were stored in MRB80 buffer (80 mM Pipes pH 6.8, 1 mM $MgCl_2$, 1 mM EGTA) supplemented with 10% glycerol.

Coverslips were plasma cleaned using Carbon Coater (Agar Scientific) and treated with PlusOne Repel-Silane (GE Healthcare) for 10–15 min. The coverslips were further cleaned by sonication in methanol and finally rinsed in water. Flow chambers were assembled with cleaned coverslips and microscopy slides using double-sided tape.

The chambers were treated with 0.2 mg/ml PLL-PEG-biotin (Surface solutions, Switzerland) in MRB80 buffer for 5 min. Subsequently they were washed with buffer and incubated with 1 mg/ml NeutrAvidin (Thermo Fisher) for 5 min. MT seeds were attached to the coverslips with the biotin-NeutrAvidin links and then incubated with NeutrAvidin once again to neutralize the exposed biotins on MT seeds that were already bound to coverslips. Finally, the chambers were incubated with 1 mg/ml κ-casein.

The *in vitro* reaction mixture was prepared in MRB80 buffer (80 mM Pipes pH 6.8, 1 mM $MgCl_2$, 1 mM EGTA) consisting of 12 µM tubulin mix (11.5 µM unlabelled-tubulin and 0.5 µM rhodamine-tubulin), 50–60 mM KCl, 2 mM $MgCl_2$, 0.1% Methylcellulose, 0.5 mg/ml κ-casein, 1 mM GTP, 6 mM DTT, oxygen scavenging system (400 µg/ml glucose-oxidase, 200 µg/ml catalase, 4 mM DTT and 20 mM glucose) and 10 nM of relevant Dam1C proteins. The mixture was centrifuged for 5 min using Airfuge. To the supernatant, nanobeads coated with Ndc80C-GFP or Ndc80C-His were mixed and added to the flow chamber containing MT seeds. The chamber was sealed with vacuum grease and observed at 30 °C by TIRF microscopy. To study behaviour of Dam1C on dynamic MTs, the reaction mixture was prepared in the same way as above but without nanobeads.

TIRF Microscopy and Image analysis

Images of dynamic MTs were acquired by TIRF microscopy using Nikon Eclipse Ti-E (Nikon) inverted research microscope equipped with four diode lasers (405 nm, 488 nm, 561 nm, 647 nm; Coherent), AOTF shutter (Solamere Technology), appropriate filters (Chroma), perfect focus system, the CFI Apochromat TIRF 100X 1.49 N.A. oil objective lens (Nikon) and Evolve Detla EMCCD 512x512 camera (Photometrics). The TIRF system was controlled with µ-manager software (Open Imaging) [31]. A temperature control chamber (Okolab) was used to maintain the temperature.

Images were analysed using ImageJ and OMERO. Kymographs were generated in time sequence along a chosen line for an individual MT, using KymoResliceWide plugin on ImageJ. The Dam1C-GFP intensity at the end of depolymerizing MT was obtained from Kymographs along the path of the MT depolymerisation, using imageJ. Statistical analyses in Figures 1, 2 and 3 were carried out with Prism software (GraphPad), using Fishers exact test. The fluorescence intensity of GFP protein and that of Ndc80C-GFP on nanobeads were obtained from TIRF microscopy images (in semi TIRF angle) using ImageJ plugin DoM (Detection of Molecules, https://github.com/ekatrukha/DoM_Utrecht). All the experiments were repeated at least twice and similar results were obtained.

Mathematical simulation of error correction

The simulation is based on a sequence of states, as shown in Figure S3A. Each state is defined by the combination of attachments between the two sister kinetochores (A and B) and MTs (up to two per kinetochore) extending from the spindle poles (L and R). There are two possible MT–kinetochore attachments: lateral and end-on. The next state is generated from the current state, based on pre-defined rules, illustrated in Figure S3A. The time required for transition from one state to another is defined with a transition rate, R, on the Poisson law. Each transition time is generated from the exponential distribution with a cumulative distribution of $F(t;R) = 1 - e^{-Rt}$, where t is time. The sequence of states is generated for each kinetochore independently. We consider two model variants (Models 1 and 2), based on two different sets of rules. In both models, the initial state is syntelic attachment to the left spindle pole, i.e. both sister kinetochores (A and B) forming end-on attachment to MTs from the left spindle pole, based on the evidence that syntelic attachment is predominant when bipolar spindle is established in budding yeast [5]. Figure S3A shows the sequence of states for sister kinetochore A; the initial state is end-on attachment to the left spindle pole. The states can occur in the same way for sister kinetochore B independently.

Model 1: generation of unattached kinetochores
In this model variant we assume that the end-on attachment can be detached spontaneously, which generates a kinetochore unattached to a MT. The sequence of states for this model is shown in Figure S3A (Model 1). Let us first consider an end-on attachment to the left spindle pole, as the simulation starts with syntelic attachment to the left. Subsequently, the end-on attachment is removed at a detachment rate, R_{det}. Next, a lateral attachment is established at

a formation rate, R_{form}; the direction of this attachment (left or right spindle pole) is chosen at random with equal probability. Then, the lateral attachment is converted to an end-on attachment at a conversion rate, R_{conv}. This sequence of three states is repeated at each kinetochore independently until the final bi-orientation is achieved. The final state is defined by both kinetochores in the end-on state attached to MTs from opposite spindle poles.

Model 2: replacement of end-on attachment by lateral attachment
In this model variant we assume that the end-on attachment can be only removed by replacing it with a lateral attachment from the opposite SPB. The sequence of states is shown in Figure S3A (Model 2). We first consider an end-on attachment to the left spindle pole, as the simulation starts with syntelic attachment to the left. Subsequently a lateral attachment forms on top of this at a replacement rate, R_{repl}. The direction of this new attachment (left or right spindle pole) is chosen at random with equal probability. If the MT comes from the opposite spindle pole, it will take over the existing end-on attachment by forming an ambilink attachment (MTs originating from opposite sites forming end-on and lateral attachments), from which the end-on attachment is knocked off at a rate R_{ko}. A single lateral attachment remains and is then converted to an end-on attachment from the opposite spindle pole at a conversion rate, R_{conv}. If the lateral MT comes from the same spindle pole, then the takeover fails. A synlink attachment (MTs originating from the same side forming end-on and lateral attachments) is formed and converted to the end-on attachment at the rate R_{conv}. This, in turn creates a dual bi-end attachment, where the second MT is quickly knocked off at the rate R_{ko}, to form a single end-on attachment identical to the initial state. In summary, a successful lateral takeover changes the end-on attachment side, whereas an unsuccessful one doesn't.

Parameter values
We estimated parameter values as follow: R_{form} and R_{rep} were evaluated as 2 min^{-1} since the half-life of kinetochore capture by a MT extending from spindle poles was approximately 30 seconds [22]. R_{ko} was evaluated as 10 min^{-1} since an Ndc80C–nanobead maintained both end-on and lateral attachment for 4–8 seconds before end-on attachment is disrupted in the presence of Dam1C-4D (Figure 2). Evaluations of R_{conv} and R_{det} are described in the next paragraphs.
Conversion rate: We estimated the conversion rate, R_{conv}, using the agent-based simulation that tracks detailed 3D interactions between MTs and kinetochores ([22, 23]). We ran the simulation 3000 times with the default parameters, as in [22] and recorded the time from the onset of the lateral attachment until the formation of the end-on attachment, each time this happened to any of the kinetochores (Figure S3B). The resulting distribution of conversion times has the mean of 0.488 min, which corresponds to a rate of 2.05 min^{-1}. Following this result, we use the conversion rate of R_{conv} = 2 min^{-1}.
Detachment rate: The value for the kinetochore detachment rate, R_{det} , is unknown and difficult to estimate. Therefore we varied this value between 0.0625 and 4 min^{-1} (Figure S3C). With each value, we ran simulation (Model 1) and obtained distribution of time required for bi-orientation. Among the values we tried, 1 min^{-1} gave the shortest median time. So, in this study, we use the kinetochore detachment rate of R_{det} = 1 min^{-1}, with which bi-orientation can be established most efficiently in Model 1.

Model runs and data presentation
We ran the simulation 10,000 times for each set of parameters in consideration, both for model variants Model 1 and 2. We started each simulation run with a syntelic configuration, where both kinetochores were end-on attached to the same (left) spindle pole. Each simulation was allowed to run until the correct bi-orientation was achieved, after which we recorded the time required to reach the final configuration. We also recorded a detailed sequence of states for a small number of simulations, to show as representative examples (Figure S3D). To show relative frequency in graphs (Figure 4B, D and S3B), the density plot was used, i.e. the y-axis was labelled in such a way that the total area of all bars (the sum of a bin size [in min] multiplied by height of each bar) is 1.

Code availability
The simulation code is written in R and available, together with detailed description and development history, on GitHub (https://github.com/bartongroup/MG_KinErr).

Live-cell imaging of yeast cells

T12419 *Saccharomyces cerevisiae* strain (W303 derivative with *CEN5-tetOs, TetR-GFP* and *SPC42-mCherry*) was generated by bringing the constructs *CEN5-tetOs* [32], *TetR-GFP* [33], *SPC42-mCherry* [34] together to one haploid strain by crossing yeast strains carrying each construct [35]. The T12419 cells were cultured at 25ºC in YPA medium containing 2% glucose (YPAD) [35], and synchronized in the cell cycle, by treating them with α factor and releasing them to fresh media.

During time-lapse imaging, yeast cells were immobilized on a glass-bottomed dish (MatTek, P35G-1.5-10-C) coated with concanavalin A (Sigma C7275), and maintained in SC plus YPA medium (3:1 ratio) [35, 36]. Images were acquired every 20 seconds using a DeltaVision Elite microscope (Applied Precision), an UPlanSApo 100× objective lens (Olympus; NA 1.40), SoftWoRx software (Applied Precision), and a CoolSnap HQ (Photometrics). Seven z-sections (0.7 µm apart) were acquired, which were subsequently processed by deconvolution, and analysed using Volocity (Improvision) software. GFP and mCherry signals were discriminated using the 89006 multi-band filter set (Chroma). For the image panels in Figures, Z sections were projected to two-dimensional images.

The *CEN5* location was classified as shown in diagrams at bottom of Figure S4A. Mother and daughter SPBs were distinguished based on the intensity of SPB signal (mother SPB usually showed more intense signals [37]). When *CEN5* signals (non-separated) totally or partially overlapped with mother and daughter SPB signals, the patterns were defined as blue and red, respectively. When *CEN5* signals (non-separated) were present between two SPBs, the pattern was defined as orange. When *CEN5* signals showed separation or stretching between two SPBs, the pattern was defined as yellow. Rare cases, where *CEN5* (non-separated) – SPB1 – SPB2 makes an obtuse angle, were defined as blue or red (depending on which SPB was closer to *CEN5*) even if *CEN5* and SPB signals did not overlap. When the yellow or orange patterns continued for 3 or more consecutive time points, the first of such time points was defined as timing of bi-orientation establishment, unless these consecutive time points were followed by a larger number of consecutive time points of blue or red.

References

1. Tanaka, T.U. (2010). Kinetochore-microtubule interactions: steps towards bi-orientation. The EMBO journal *29*, 4070-4082.
2. Rieder, C.L., and Alexander, S.P. (1990). Kinetochores are transported poleward along a single astral microtubule during chromosome attachment to the spindle in newt lung cells. The Journal of cell biology *110*, 81-95.
3. Tanaka, K., Mukae, N., Dewar, H., van Breugel, M., James, E.K., Prescott, A.R., Antony, C., and Tanaka, T.U. (2005). Molecular mechanisms of kinetochore capture by spindle microtubules. Nature *434*, 987-994.
4. Tanaka, K., Kitamura, E., Kitamura, Y., and Tanaka, T.U. (2007). Molecular mechanisms of microtubule-dependent kinetochore transport toward spindle poles. The Journal of cell biology *178*, 269-281.
5. Tanaka, T.U., Rachidi, N., Janke, C., Pereira, G., Galova, M., Schiebel, E., Stark, M.J., and Nasmyth, K. (2002). Evidence that the Ipl1-Sli15 (Aurora kinase-INCENP) complex promotes chromosome bi-orientation by altering kinetochore-spindle pole connections. Cell *108*, 317-329.
6. Hauf, S., Cole, R.W., LaTerra, S., Zimmer, C., Schnapp, G., Walter, R., Heckel, A., Van Meel, J., Rieder, C.L., and Peters, J.M. (2003). The small molecule Hesperadin reveals a role for Aurora B in correcting kinetochore-microtubule attachment and in maintaining the spindle assembly checkpoint. The Journal of cell biology *161*, 281-294.
7. Lampson, M.A., Renduchitala, K., Khodjakov, A., and Kapoor, T.M. (2004). Correcting improper chromosome-spindle attachments during cell division. Nature cell biology *6*, 232-237.
8. Cheeseman, I.M., Anderson, S., Jwa, M., Green, E.M., Kang, J., Yates, J.R., 3rd, Chan, C.S., Drubin, D.G., and Barnes, G. (2002). Phospho-regulation of kinetochore-microtubule attachments by the Aurora kinase Ipl1p. Cell *111*, 163-172.
9. Kalantzaki, M., Kitamura, E., Zhang, T., Mino, A., Novak, B., and Tanaka, T.U. (2015). Kinetochore-microtubule error correction is driven by differentially regulated interaction modes. Nat Cell Biol. *17*, 421-433.
10. Sarangapani, K.K., Akiyoshi, B., Duggan, N.M., Biggins, S., and Asbury, C.L. (2013). Phosphoregulation promotes release of kinetochores from dynamic microtubules via multiple mechanisms. Proc Natl Acad Sci U S A. *110*, 7282-7287.
11. Cheeseman, I.M., Chappie, J.S., Wilson-Kubalek, E.M., and Desai, A. (2006). The conserved KMN network constitutes the core microtubule-binding site of the kinetochore. Cell *127*, 983-997.
12. Wei, R.R., Al-Bassam, J., and Harrison, S.C. (2007). The Ndc80/HEC1 complex is a contact point for kinetochore-microtubule attachment. Nat Struct Mol Biol *14*, 54-59.
13. Ciferri, C., Pasqualato, S., Screpanti, E., Varetti, G., Santaguida, S., Dos Reis, G., Maiolica, A., Polka, J., De Luca, J.G., De Wulf, P., et al. (2008). Implications for kinetochore-microtubule attachment from the structure of an engineered Ndc80 complex. Cell *133*, 427-439.
14. Gonen, S., Akiyoshi, B., Iadanza, M.G., Shi, D., Duggan, N., Biggins, S., and Gonen, T. (2012). The structure of purified kinetochores reveals multiple microtubule-attachment sites. Nat Struct Mol Biol *19*, 925-929.
15. Westermann, S., Wang, H.W., Avila-Sakar, A., Drubin, D.G., Nogales, E., and Barnes, G. (2006). The Dam1 kinetochore ring complex moves processively on depolymerizing microtubule ends. Nature *440*, 565-569.
16. Keating, P., Rachidi, N., Tanaka, T.U., and Stark, M.J. (2009). Ipl1-dependent phosphorylation of Dam1 is reduced by tension applied on kinetochores. J Cell Sci *122*, 4375-4382.
17. Lampert, F., Hornung, P., and Westermann, S. (2010). The Dam1 complex confers microtubule plus end-tracking activity to the Ndc80 kinetochore complex. The Journal of cell biology *189*, 641-649.
18. Tien, J.F., Umbreit, N.T., Gestaut, D.R., Franck, A.D., Cooper, J., Wordeman, L., Gonen, T., Asbury, C.L., and Davis, T.N. (2010). Cooperation of the Dam1 and Ndc80

kinetochore complexes enhances microtubule coupling and is regulated by aurora B. The Journal of cell biology *189*, 713-723.

19. Kim, J.O., Zelter, A., Umbreit, N.T., Bollozos, A., Riffle, M., Johnson, R., MacCoss, M.J., Asbury, C.L., and Davis, T.N. (2017). The Ndc80 complex bridges two Dam1 complex rings. eLife *6*. e21069
20. Zelter, A., Bonomi, M., Kim, J., Umbreit, N.T., Hoopmann, M.R., Johnson, R., Riffle, M., Jaschob, D., MacCoss, M.J., Moritz, R.L., et al. (2015). The molecular architecture of the Dam1 kinetochore complex is defined by cross-linking based structural modelling. Nature communications *6*, 8673.
21. Legal, T., Zou, J., Sochaj, A., Rappsilber, J., and Welburn, J.P. (2016). Molecular architecture of the Dam1 complex-microtubule interaction. Open biology *6*.
22. Vasileva, V., Gierlinski, M., Yue, Z., O'Reilly, N., Kitamura, E., and Tanaka, T.U. (2017). Molecular mechanisms facilitating the initial kinetochore encounter with spindle microtubules. The Journal of cell biology *216*, 1609-1622.
23. Yue, Z., Komoto, S., Gierlinski, M., Pasquali, D., Kitamura, E., and Tanaka, T.U. (2017). Mechanisms mitigating problems associated with multiple kinetochores on one microtubule in early mitosis. J Cell Sci *130*, 2266-2276.
24. Gandhi, S.R., Gierlinski, M., Mino, A., Tanaka, K., Kitamura, E., Clayton, L., and Tanaka, T.U. (2011). Kinetochore-dependent microtubule rescue ensures their efficient and sustained interaction in early mitosis. . Developmental cell *21*, 920-933.
25. Maure, J.F., Komoto, S., Oku, Y., Mino, A., Pasqualato, S., Natsume, K., Clayton, L., Musacchio, A., and Tanaka, T.U. (2011). The Ndc80 loop region facilitates formation of kinetochore attachment to the dynamic microtubule plus end. Current biology *21*, 207-213.
26. Bieniossek, C., Richmond, T.J., and Berger, I. (2008). MultiBac: multigene baculovirus-based eukaryotic protein complex production. Current protocols in protein science *Chapter 5*, Unit 5.20.
27. Miranda, J.J., De Wulf, P., Sorger, P.K., and Harrison, S.C. (2005). The yeast DASH complex forms closed rings on microtubules. Nat Struct Mol Biol *12*, 138-143.
28. Gestaut, D.R., Graczyk, B., Cooper, J., Widlund, P.O., Zelter, A., Wordeman, L., Asbury, C.L., and Davis, T.N. (2008). Phosphoregulation and depolymerization-driven movement of the Dam1 complex do not require ring formation. Nature cell biology *10*, 407-414.
29. Fairhead, M., and Howarth, M. (2015). Site-specific biotinylation of purified proteins using BirA. Methods Mol Biol *1266*, 171-184.
30. Katoh, Y., Nozaki, S., Hartanto, D., Miyano, R., and Nakayama, K. (2015). Architectures of multisubunit complexes revealed by a visible immunoprecipitation assay using fluorescent fusion proteins. J Cell Sci *128*, 2351-2362.
31. Edelstein, A.D., Tsuchida, M.A., Amodaj, N., Pinkard, H., Vale, R.D., and Stuurman, N. (2014). Advanced methods of microscope control using μManager software. Journal of biological methods *1*. e10.
32. Tanaka, T., Fuchs, J., Loidl, J., and Nasmyth, K. (2000). Cohesin ensures bipolar attachment of microtubules to sister centromeres and resists their precocious separation. Nature cell biology *2*, 492-499.
33. Michaelis, C., Ciosk, R., and Nasmyth, K. (1997). Cohesins: chromosomal proteins that prevent premature separation of sister chromatids. Cell *91*, 35-45.
34. Maure, J.F., Kitamura, E., and Tanaka, T.U. (2007). Mps1 kinase promotes sister-kinetochore bi-orientation by a tension-dependent mechanism. Current biology *17*, 2175-2182.
35. Amberg, D.C., Burke, D.J., and Strathern, J.N. (2005). Methods in yeast genetics.
36. Tanaka, K., Kitamura, E., and Tanaka, T.U. (2010). Live-cell analysis of kinetochore-microtubule interaction in budding yeast. Methods *51*, 206-213.
37. Pereira, G., Tanaka, T.U., Nasmyth, K., and Schiebel, E. (2001). Modes of spindle pole body inheritance and segregation of the Bfa1p-Bub2p checkpoint protein complex. The EMBO journal *20*, 6359-6370.

Figure 1

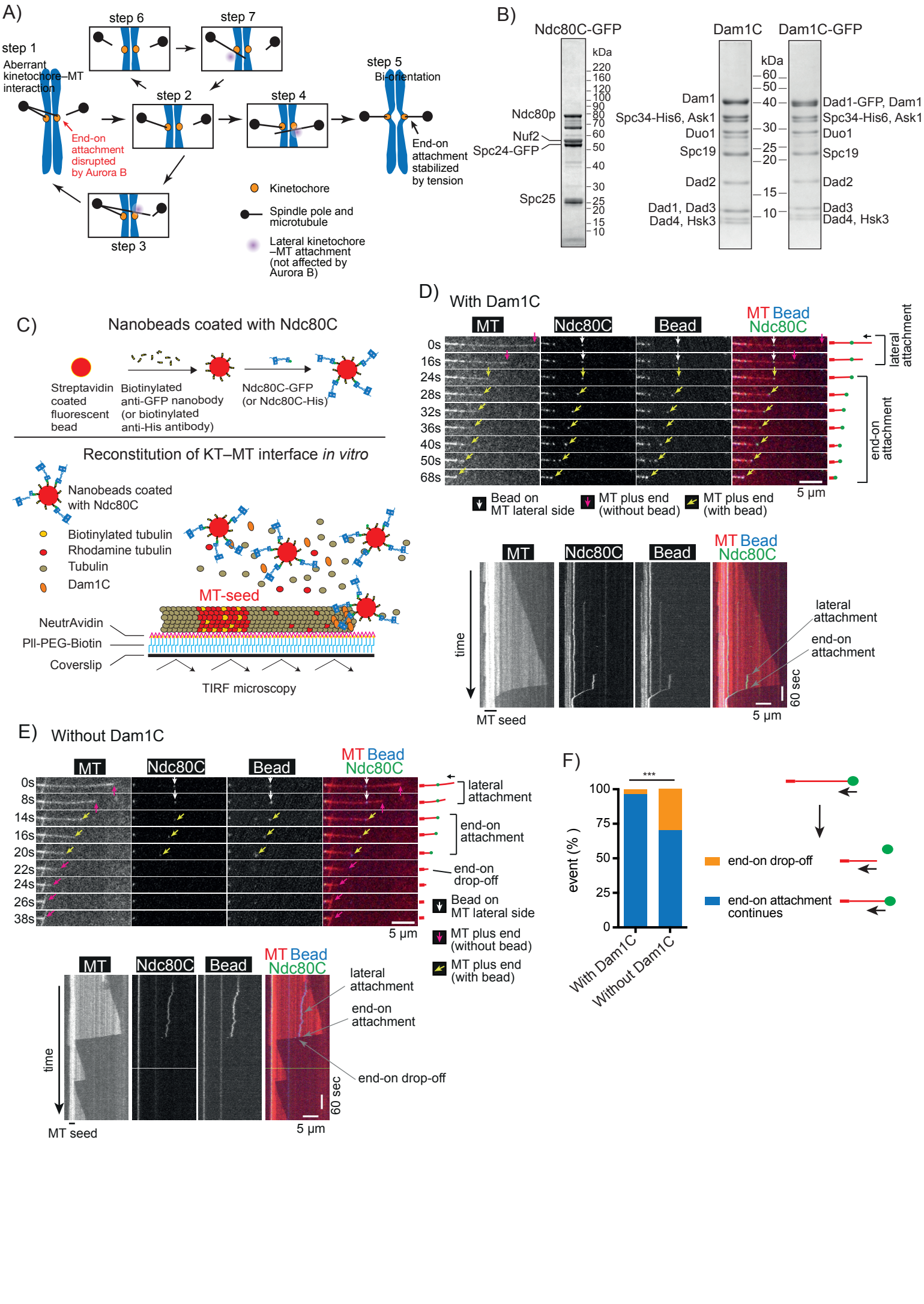

Figure 1. Behaviour of Ndc80C–nanobeads *in vitro* on dynamic MTs loaded with Dam1C.

A) Diagram shows the current view of an error correction process, proposed in [9]. Each step is explained in the text.

B) Coomassie Blue stained gels showing purified Ndc80C-GFP (with GFP at the C-terminus of Spc24), Dam1C and Dam1C-GFP (with GFP at the C-terminus of Dad1).

C) Diagram shows that Ndc80C-GFP was attached to a streptavidin-coated nanobead through a biotinylated anti-GFP nanobody (top). Dynamic MTs were grown on coverslips in the presence of Dam1C and Ndc80C-GFP-coated nanobeads (Ndc80C–nanobeads), and observed by TIRF microscopy (bottom).

D) Images in time sequence (top) show that an Ndc80C–nanobead formed MT lateral attachment (0–16 s time points) and end-on attachment (24–68 s) in the presence of Dam1C. Time 0 s was set arbitrarily. Scale bar, 5 μm. Also refer to diagrams (right). Kymograph was obtained for the same MT (bottom). Scale bars, 5 μm (horizontal) and 60 s (vertical).

E) Images in time sequence (top) show that an Ndc80C–nanobead formed MT lateral attachment (0–8 s) and end-on attachment (14–20 s), and subsequently detached from the MT end (end-on drop-off; 22 s), in the absence of Dam1C. After the nanobead had detached from the MT end, it was not visible by TIRF microscopy because it was no longer close to the coverslip. Also refer to diagrams (right). Kymograph was obtained for the same MT (bottom). Scale bars are as in D).

F) Graph shows the percentage of events; end-on drop-off and continuous end-on attachment, observed in the presence (n=82) and absence (n=30) of Dam1C. Difference between the two groups is significant (p=0.0003).

Figure 2

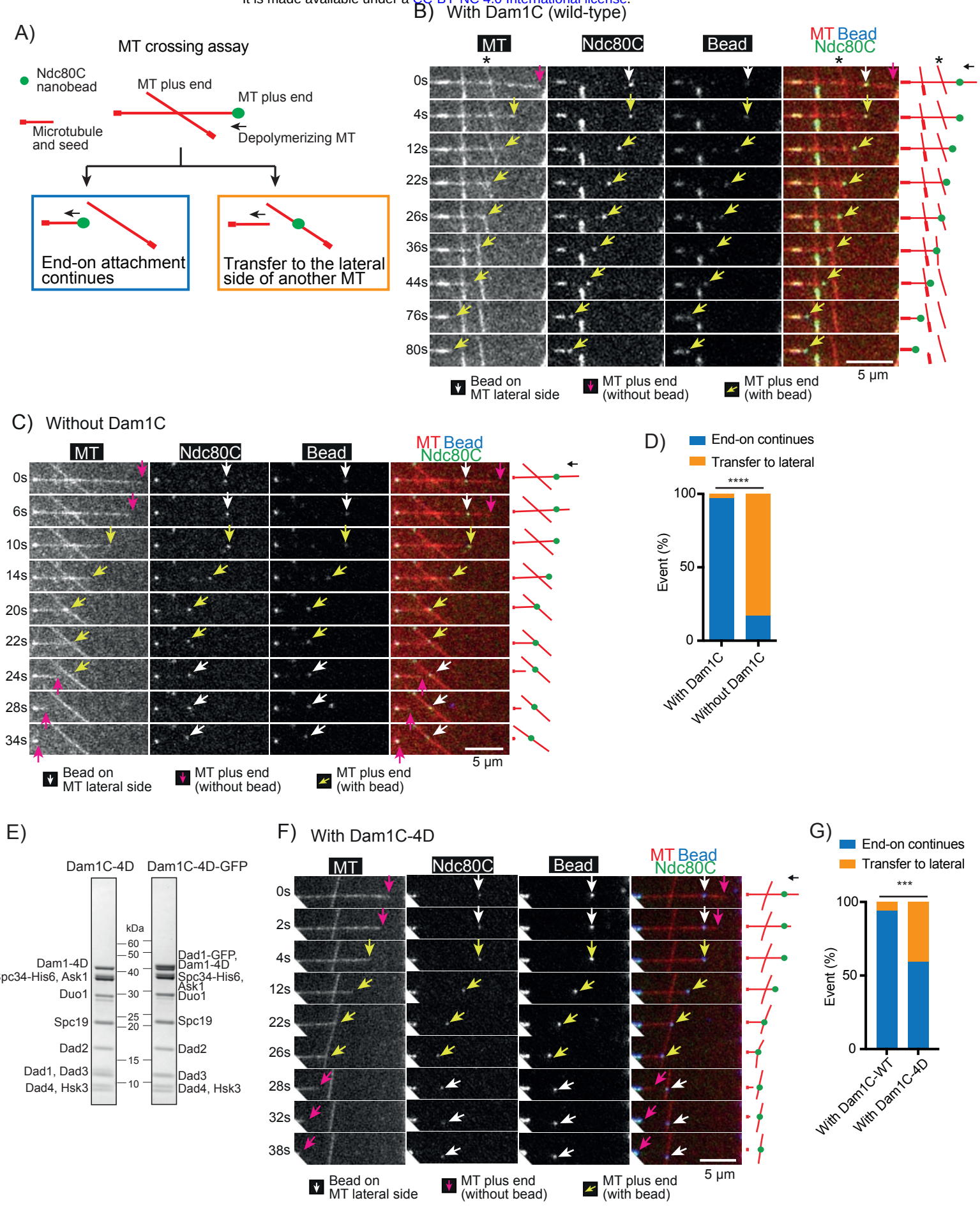

Figure 2. End-on attachment on one MT and lateral attachment on another are in direct competition for Ndc80C–nanobeads.

A) Diagram explains the MT crossing assay. Two MTs cross each other, one of which forms end-on attachment to the Ndc80C–nanobead and depolymerizes. Two possible outcomes are shown; i) end-on attachment continues (blue rectangle) or ii) the Ndc80C–nanobead is transferred to the side of the other MT (orange rectangle).

B) Images in time sequence show that the MT end-on attachment to the Ndc80C–nanobead continued after it had passed over the lateral side of another MT, in the presence of Dam1C. Time 0 s was set arbitrarily. Scale bar, 5 μm. Also refer to diagrams (right). Asterisk indicates a crossing MT.

C) Images in time sequence show that an Ndc80C–nanobead was transferred from the end of one MT to the side of another MT, in the absence of Dam1C. Time 0 s was set arbitrarily. Scale bar, 5 μm. Also refer to diagrams (right).

D) Percentage of events in the MT crossing assay in the presence and absence of Dam1C (n=35 for each); i) continued end-on attachment of Ndc80C–nanobead (blue) and ii) transfer to the lateral side of another MT (orange). These events are shown in diagram A, inside the rectangles of the same colour. Difference between the two groups is significant (p<0.0001).

E) Coomassie Blue stained gel showing purified Dam1C-4D (in which four serine residues at the C-terminus of Dam1 were replaced with aspartate) with and without GFP at the C-terminus of Dad1.

F) Images in time sequence show that an Ndc80C–nanobead was transferred from the end of one MT to the lateral side of another MT in the presence of Dam1C-4D. Scale bar, 5 μm. Also refer to diagrams (right).

G) Percentage of events in the MT crossing assay with Dam1C wild-type (WT) and Dam1C-4D (n=34 and 44, respectively); i) continued end-on attachment (blue) and ii) transfer to the lateral side of another MT (orange). These events are shown in diagram A, inside the rectangles of the same colour. Difference between the two groups is significant (p=0.0005).

Figure 3

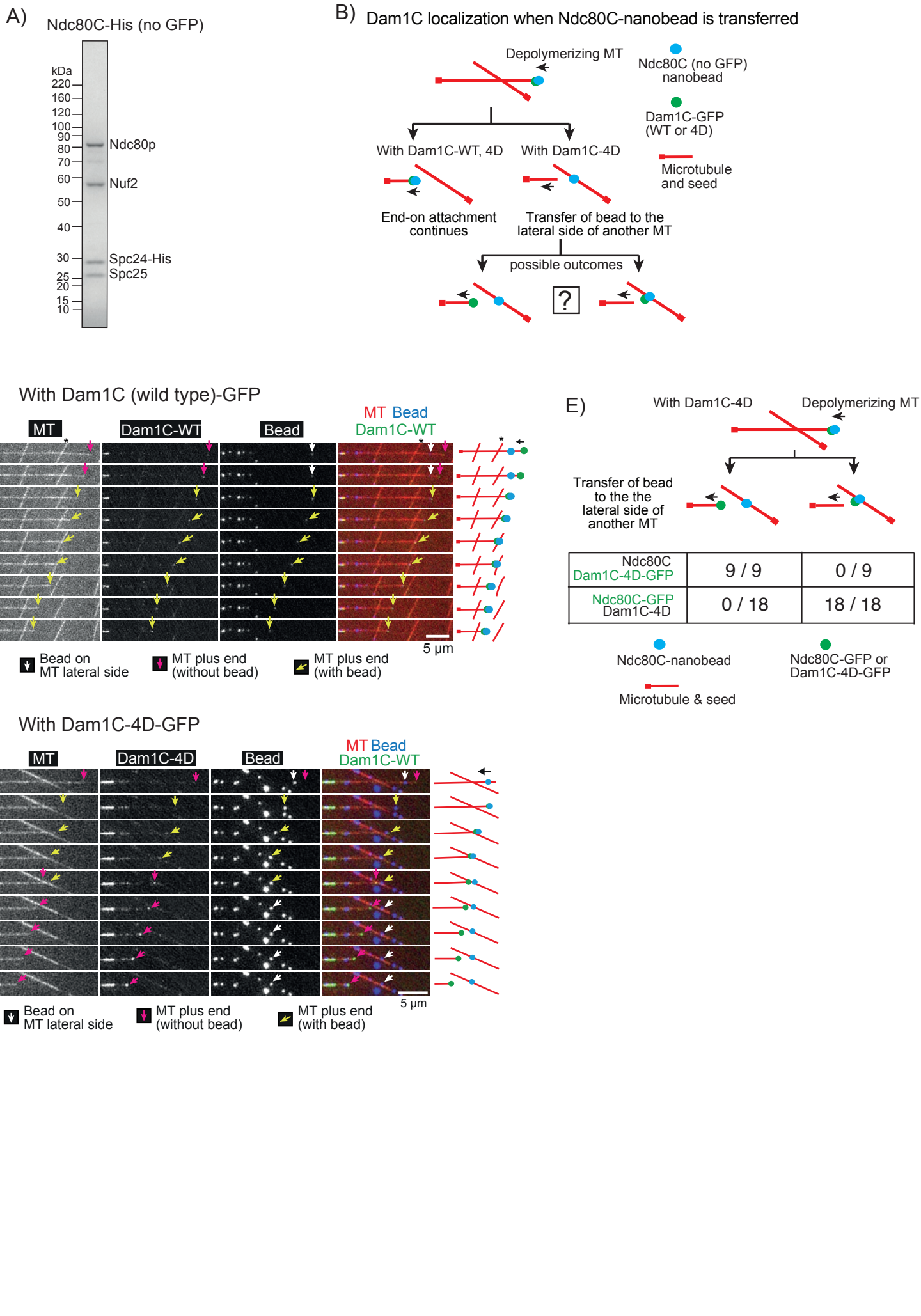

Figure 3. Dam1C-4D disrupts the interaction with Ndc80C, leading to transfer of an Ndc80C–nanobead to the side of another MT.

A) Coomassie Blue stained gel showing purified Ndc80C-His (without GFP and with His-tag at the C-terminus of Spc24).

B) Diagrams explains various outcomes in the MT crossing assay regarding the position of an Ndc80C–nanobead and the location of Dam1C-GFP (wild-type or 4D) signals.

C) Images in time sequence show that the MT end-on attachment to an Ndc80C–nanobead continued after it had passed across the side of another MT in the presence of Dam1C (wild-type)-GFP. Dam1C (wild-type)-GFP signals were at the end of the depolymerizing MT with nanobead throughout the end-on attachment. Time 0 s was set arbitrarily. Scale bar, 5 μm. Also refer to diagrams (right). Asterisk indicates a crossing MT.

D) Images in time sequence show that an Ndc80C–nanobead was transferred from the end of one MT to the side of another MT in the presence of Dam1C-4D-GFP. Dam1C-4D-GFP signals tracked the end of depolymerizing MT, moving away from the Ndc80C–nanobead. Time 0 s was set arbitrarily. Scale bar, 5 μm. Also refer to diagrams (right).

E) Frequency of events in the MT crossing assay. The cases where Ndc80C–nanobeads were transferred to the lateral side of another MT, with Ndc80C (no GFP) and Dam1-4D-GFP or with Ndc80C-GFP and Dam1C-4D (no GFP), were investigated. After transfer of the nanobead to the lateral side of another MT, Dam1-4D-GFP always tracked the end of the original MT (9 out of 9 events) while Ndc80C-GFP always located at the nanobead (18 out of 18 events). Difference between Dam1-4D-GFP and Ndc80C-GFP is significant ($p<0.0001$).

Figure 4

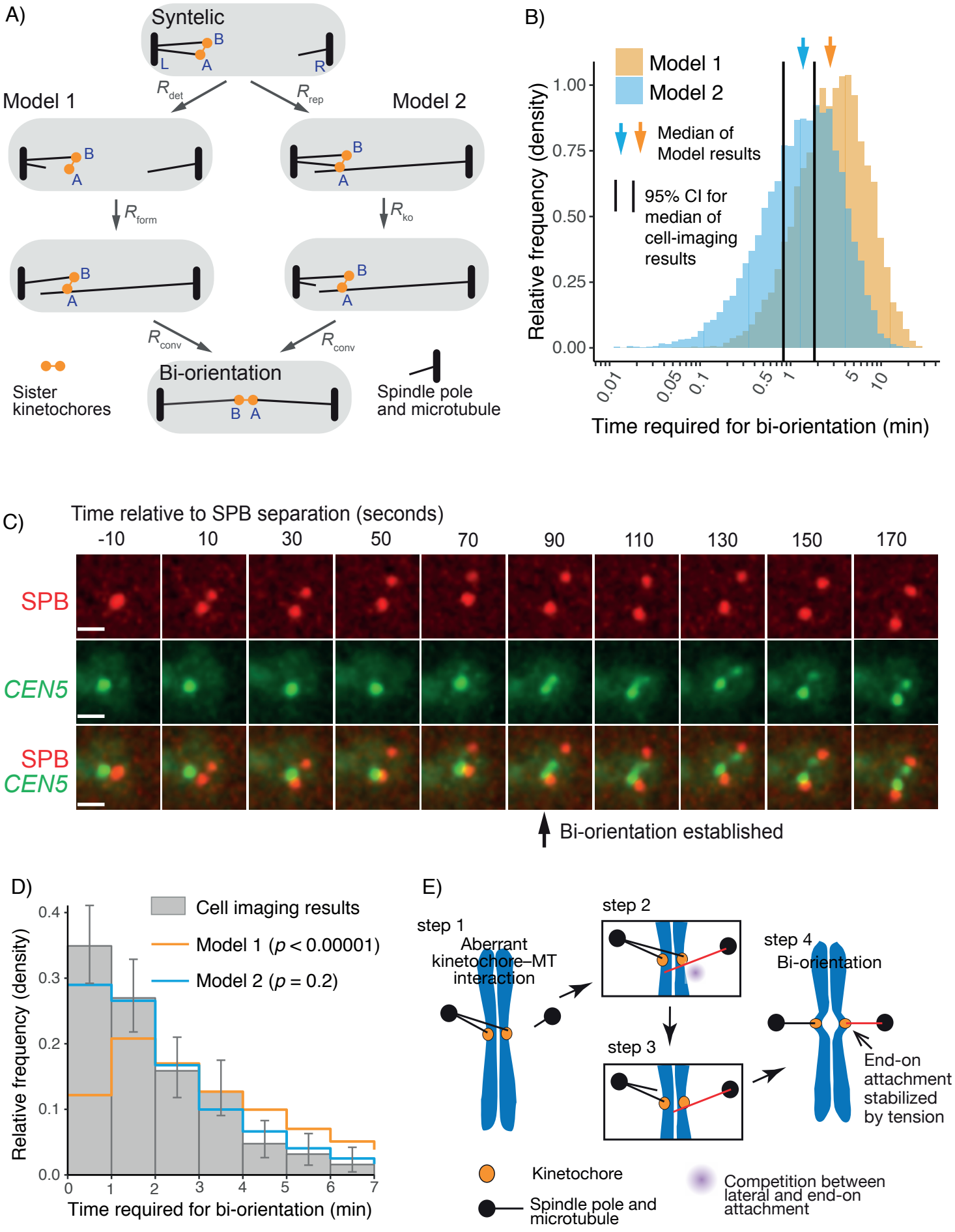

Figure 4. Error correction through direct competition between end-on and lateral attachment explains efficient establishment of bi-orientation in cells.

A) Mathematical simulations of error correction based on two models: In Model 1, the error correction proceeds through generation of unattached kinetochores. In Model 2, it proceeds through direct competition between end-on and lateral attachment. In the diagram, A and B represent each sister kinetochore, while L and R show the left and right spindle pole, respectively. The diagram shows the simplest error correction processes leading to bi-orientation in each model. All possible sequences of states for sister kinetochore A are shown in Figure S3A. Though sister kinetochore B does not show any turnover of MT attachments in this diagram (to simplify the diagram), B could show the turnover, independently of sister kinetochore A, in simulations.

B) Graph shows distribution of time required for bi-orientation in simulations with Model 1 (light orange bars) and Model 2 (light blue bars). The median times are shown in arrows. Black lines show the 95% confidence interval (CI) for the median time required for bi-orientation in live-cell imaging (C and D).

C) Images show a representative example of live-cell imaging. T12419 *Saccharomyces cerevisiae* cells (*CEN5-tetOs, TetR-GFP SPC42-mCherry*) were arrested with α factor treatment and released to fresh media. Images were acquired every 20 s. Time 0 s is defined as the time of SPB separation; i.e. SPB showed separation at +10 s but not at -10 s. Sister *CEN5* separation (or *CEN5* movement to the middle between two SPBs followed by sister *CEN5* separation) was marked as establishment of bi-orientation if sister *CEN5* separation continued thereafter. In the example shown here, we judged that bi-orientation was established at +90 s.

D) Graph (gray bars) shows distribution of time required for bi-orientation in live-cell imaging (63 cells). Error bars show 68% binominal CI. Distributions in simulations with Model 1 (orange line) and Model 2 (light blue line) are also shown for comparison. The *p* value for each model was obtained by Kolmogorov-Smirnov test in comparison with the live-cell imaging result.

E) Diagram shows a proposed new process of error correction based on Model 2 in A. Aberrant kinetochore–MT interaction; sister kinetochores attach to MTs from the same spindle pole (step 1). The end-on and lateral attachments to MTs from opposite poles compete for the right-hand kinetochore (step 2). Phosphorylation of kinetochore components (such as Dam1C) by Aurora B weakens the end-on attachment but not lateral attachment, leading to loss of the end-on attachment (step 3). The lateral attachment is then converted to end-on attachment, thus establishing bi-orientation. Tension is applied across sister kinetochores, stabilizing the end-on attachments on both sister kinetochores (step 4).

Supplemental Figures

Figure S1

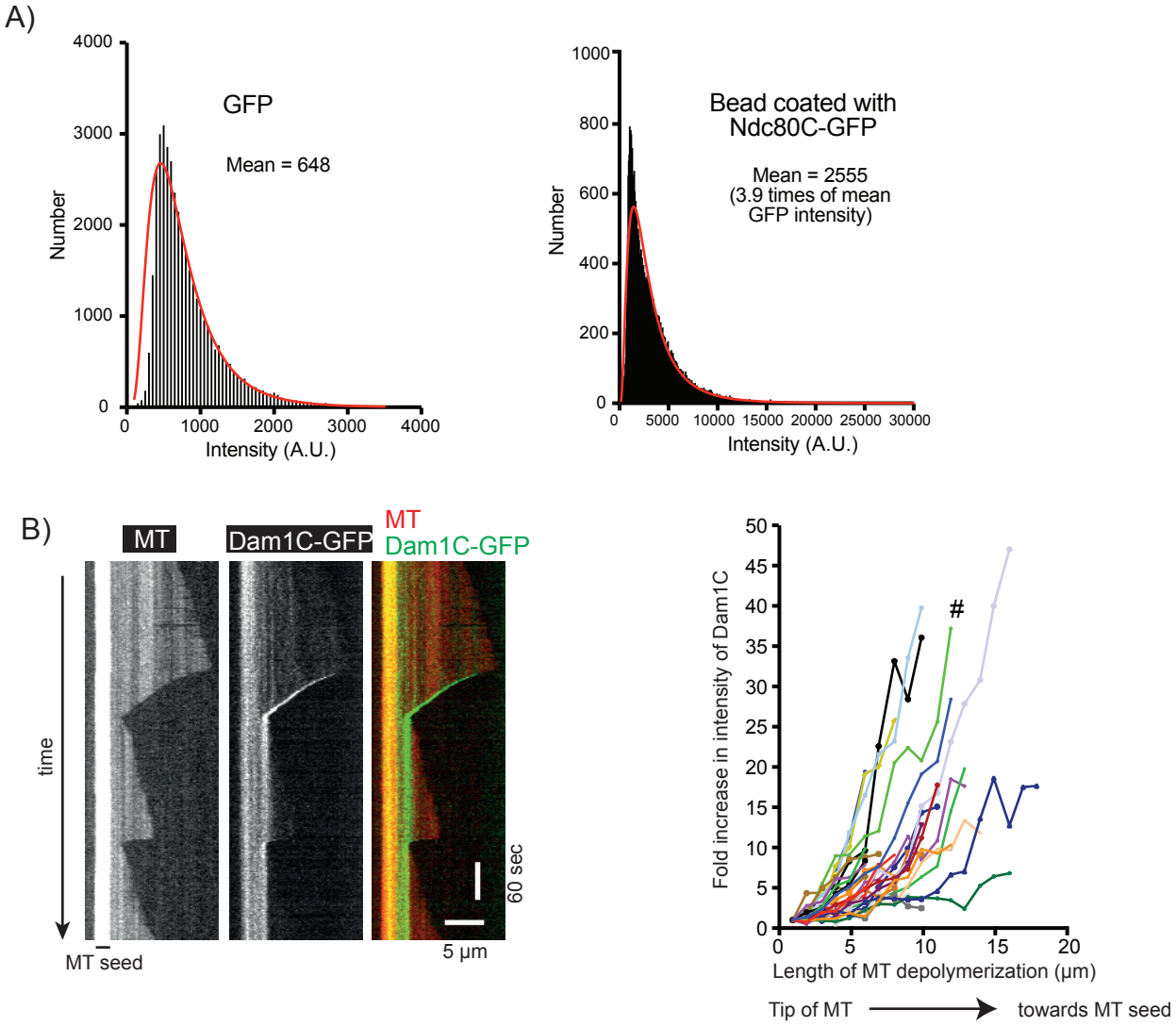

Figure S1. Supplemental data associated with Figure 1.

A) Signal quantification of GFP (by itself, not fused to Ndc80C) and Ndc80C-GFP-coated beads. Black bars (bin size 50) represent the number of fluorescent spots with the indicated intensity. The red line is the lognormal fit of the quantification. A.U., arbitrary unit.

B) Kymograph (left) shows that the Dam1C-GFP signal tracked the end of a depolymerizing MT. Scale bars, 5 μm (horizontal) and 60 s (vertical). Graph (right) shows fold increases of Dam1C-GFP signals at the plus ends of individual MTs. The Dam1C-GFP signal for the first 1 μm after their appearance was averaged and set to one for normalization. The Dam1C signal during subsequent MT shrinkage was averaged in 1-μm increments, normalized and plotted against the length of MT shrinkage. # shows the fold increase of the example shown in the kymograph (left).

Figure S2

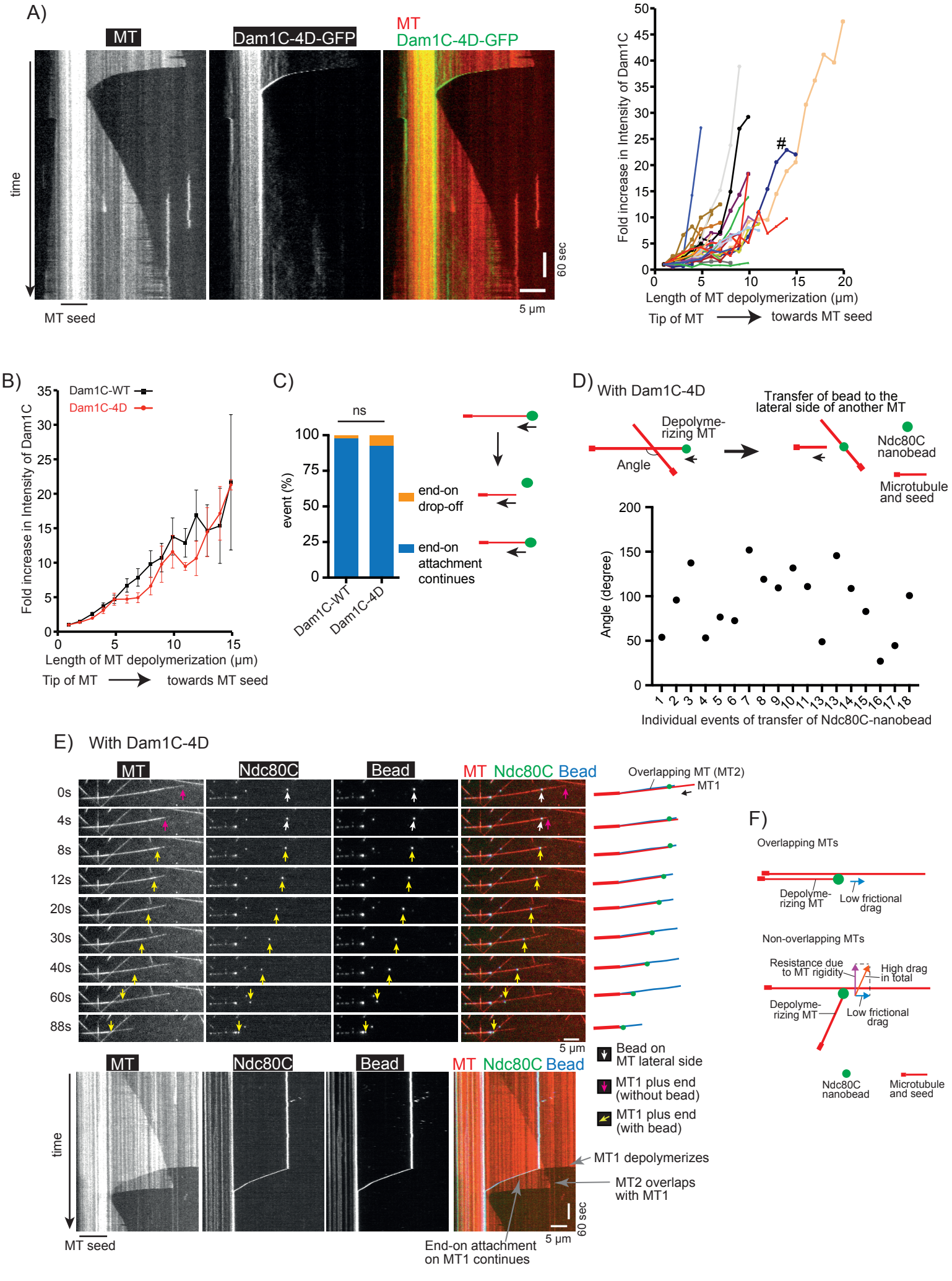

Figure S2. Supplemental data associated with Figure 2.

A) Kymograph (left) shows that Dam1C-GFP-4D signals tracked the end of a depolymerizing MT. Scale bar, 5 μm (horizontal) and 60 s (vertical). Graph (right) shows fold increases of Dam1C-GFP signals at the plus ends of individual MTs, which were obtained and plotted as in Figure S1B. # shows the fold increase in the example shown in the kymograph (left).

B) Dam1C (wild-type)-GFP and Dam1C-4D-GFP show similar fold increases at the plus end of shrinking MTs. The fold increase of Dam1C (wild-type)-GFP (n=28) (black squares) or Dam1C-4D-GFP (n=32) (red circles) signals at the shrinking MT ends (Figure S1B and S2A) was averaged among multiple MTs and plotted against the length of MT shrinkage. Error bars show SEM.

C) Graph shows the percentage of events; end-on drop-off and continuous end-on attachment, observed in the presence of Dam1C wild-type (WT) (n=122) and Dam1C-4D (n=90). Difference between the two groups is not significant (p=0.10).

D) Angles made by two MTs between which Ndc80C–nanobeads were transferred, from end-on to the lateral side of another MT, in the presence of Dam1C-4D. Angles were measured in individual events as shown in diagram (top) and plotted (bottom).

E) Images in time sequence (top) show two overlapping MTs with the same orientation (MT1 and MT2). An Ndc80C–nanobead showed an end-on attachment to MT1 (8–88 s). During this period the end-on attachment to MT1 was not lost in spite of the presence of overlapping MT2. The region where two MTs overlapped was discerned based on MT intensity, and this is clear in the kymograph (see bottom). Time 0 s was set arbitrarily. Scale bar, 5 μm. Also refer to diagram (right) where MT1 and MT2 are shown in red and blue, respectively. Kymograph was obtained for the same MTs (bottom). Scale bars, 5 μm (horizontal) and 60 s (vertical).

F) Diagrams show the forces applied on Ndc80C beads in the presence of Dam1-4D. On top, the nanobead maintains end-on attachment while it slides along an overlapping MT. We reason that, because the frictional drag (blue arrow) applied on the nanobead is low, the end-on attachment is not disrupted. At bottom, the angle between two MTs is not close to zero. As the Ndc80C bead shows higher affinity to the lateral side of a MT than to the end-on attachment, the laterally attached MT bends and a force is applied perpendicularly to it due to MT rigidity (magenta). The drag force in total (orange arrow) is larger than a frictional drag (blue arrow) along the laterally attached MT, the original end-on attachment is disrupted, and the nanobead is transferred to the lateral side of another MT.

Figure S3

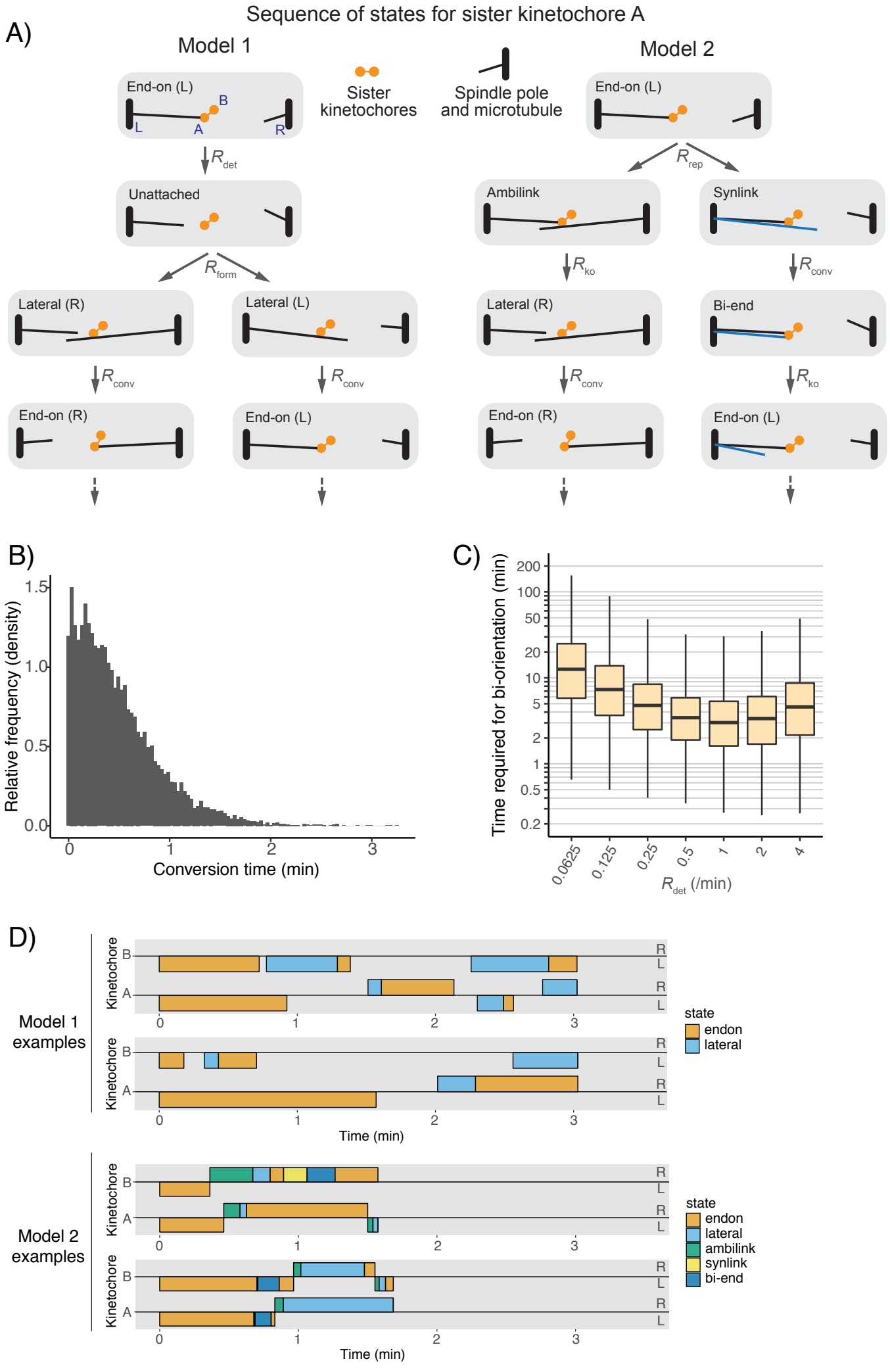

Figure S3. Supplemental data associated with Figure 4A, B.

A) Sequence of states in the mathematical simulation of error correction. All possible sequences of states are shown for sister kinetochore A with Model 1 and 2. The time required for transition from one state to another is defined by a transition rate *R*. The value for each R was obtained or optimized, as described in the text. In Synlink, Bi-end and subsequent End-on of Model 2, one MT is shown in blue to distinguish it from others. Although MT interaction with sister kinetochore B is not shown in this diagram for simplicity, sister kinetochore B can undergo a sequence of states in the same way as, and independently of, sister kinetochore A. The sequence of states finishes when sister kinetochore A and B form end-on attachment from different spindle poles. In diagrams, states of kinetochore–MT interaction are illustrated, but other aspects (e.g. the position of kinetochores) are not necessarily accurate (e.g. kinetochores are usually pulled towards a pole by MTs if bi-orientation is not established).

B) Graph shows distribution of times from formation of lateral kinetochore-MT attachment until conversion to end-on attachment on a single MT in 3000 simulations. To estimate the conversion rate, R_{conv}, we ran the agent-based simulation that tracks detailed 3D interactions between MTs and kinetochores [22, 23]. The resulting distribution of conversion times has the mean value of 0.488 min, which corresponds to a rate of 2.05 min^{-1}. Following this result, we use the conversion rate of R_{conv} = 2 min^{-1}.

C) Graph (box plots) shows distribution of times required for bi-orientation in simulations with Model 1 with various values of R_{det}. The value for the kinetochore detachment rate, R_{det} is unknown and difficult to estimate. Therefore, to optimize this value, we ran simulations (Model 1) with various values of R_{det}, and 1 min^{-1} gave the shortest median time (3.0 min). Therefore, in this study we used the kinetochore detachment rate of R_{det} =1 min^{-1}, with which bi-orientation can be established most efficiently in Model 1.

D) Diagrams show representative examples of the sequence of states in the simulation. Two examples are shown for each of Models 1 and 2. A and B designate each sister kinetochore, while R and L shows kinetochore interaction with a MT from the right and left spindle pole, respectively. Different states are shown in different colours and explained in diagrams in A. During Ambilink, one kinetochore interacts with MTs from both poles and in these diagrams it is shown at the same side of the spindle pole (R or L) as subsequent lateral attachment.

Figure S4

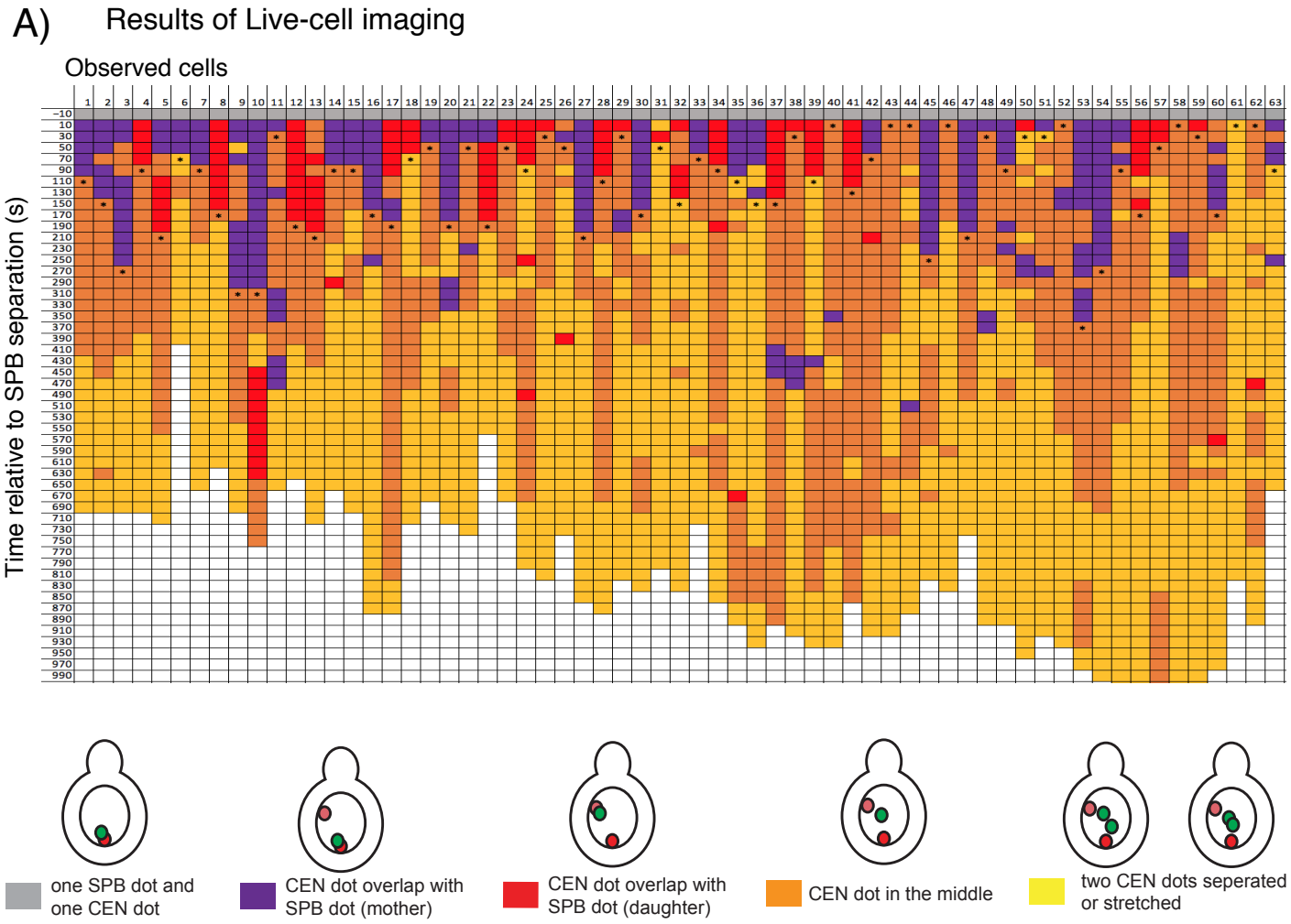

Figure S4. Supplemental data associated with Figure 4C, D.

A) Locations of *CEN5* are classified in 63 cells observed by live-cell imaging. Each column shows how the *CEN5* location changed in each cell over time. The *CEN5* location was classified as shown at the bottom of each diagram. Mother and daughter SPBs were distinguished based on the intensity of SPB signal (mother SPB usually shows more intense signals). Asterisk designates estimated time of bi-orientation establishment (see criteria in Methods). Figure 4C shows images of cell #63.